4-40 GHz Complex Permittivity Measurements of Common Building Materials

Jon W. Wallace, Rashid Mehmood, and Jonathan R. Abel

I. Introduction

This report provides details of the system and algorithms used at Brigham Young University and Lafayette College for free-space characterization of building materials in the 4-40 GHz range. The goal of this work was to extract complex permittivity of building materials with seamless coverage over the 4-40 GHz range to provide an input to detailed ray-tracing models of buildings. We were primarily interested in identifying a method that is robust to system imperfections and that can be implemented with standard microwave test equipment.

The method we have adopted is based on an equivalent network model of the test setup, requiring only transmission measurements of samples, yet providing high robustness to system imperfections. Although the method was found to be very similar to [1], [2], our approach extends these previous methods by accounting for spherical wave spreading, appropriate when using simple horns without aperture correcting lenses.

This report also documents validation efforts on the accuracy of the method for various types of materials, performed with two-dimensional (2D) method-of-moments simulations. The results indicate under what conditions good accuracy is expected, and other conditions where different measurement techniques should be employed.

Finally, results are provided herein for nine different materials, including several common building materials: drywall, concrete block, brick, plywood, oriented strand board, and window glass. These results are not only useful for corroboration with other material characterization studies, but also can be used as an input to microwave and millimeter wave (mm-wave) propagation studies and network coverage simulations.

II. Measurement System

Fig. 1(a) provides a conceptual diagram of the measurement setup we employed in this work, consisting of a two-port vector network analyzer (VNA) covering the frequency range of interest, a compact anechoic chamber to hold the sample under test, and broadband directional antennas. The material sample should be a slab placed in the center of the chamber as depicted in the figure. The basic approach, described in more detail below, is to measure the transmission response (amplitude and phase) through the material. By fitting that response to an equivalent transmission-line model, the material's complex permittivity can be estimated.

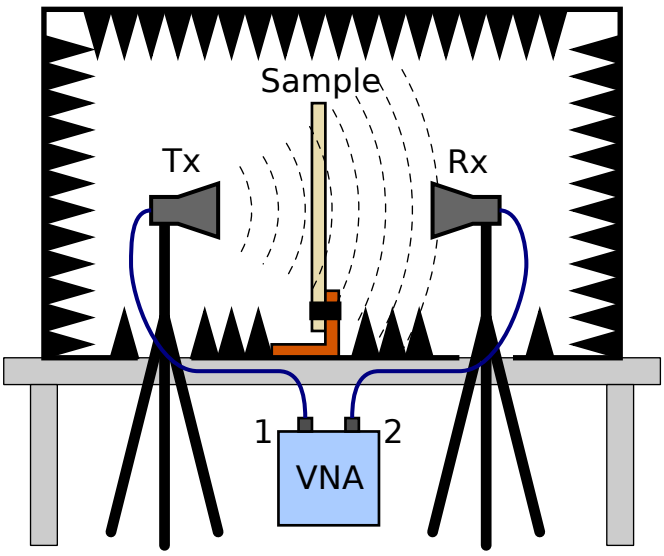

(a)

(b)

Fig. 1: Material characterization chamber used in this study: (a) schematic diagram and (b) photo of the chamber.

A. Vector Network Analyzer

The VNA computes scattering parameters (S-parameters) by exciting a forward wave with amplitude a_i on Port i at frequency f and measuring the received input wave b_j on all ports. The scattering parameter $S_{ij}(f)$ is defined as

$$S_{ij} = \left.\frac{b_j}{a_i}\right|_{a_k=0,\forall k\neq i}. \tag{1}$$

Thus, in our setup, $S_{21}(f)$ measures the transmission coefficient obtained by sending a wave out Port 1 and measuring the received incoming wave on Port 2.

For our work, we used a 4-port Rohde & Schwarz ZNB40 VNA that can operate from 0-40 GHz. Although not strictly necessary for the method, we routinely performed a full 2-port calibration (manual calibration kit) on the VNA to remove the effect of cables and connectors up to the antenna ports. For measurements reported herein, we performed a VNA sweep from 4-40 GHz, 1001 measurement points, 0 dBm transmit power, and 1 kHz resolution bandwidth.

B. Anechoic Chamber

A low-cost modular anechoic chamber was constructed for this work as depicted in Fig. 1(b). The chamber is made from generic 2×4 ft^2 carpet-covered panels, where each panel is drilled at common locations with a template, allowing the panels to be bolted together in arbitrary configurations. The carpet-backing of the panels allows Velcro-backed microwave absorber to be easily attached to the inside walls and ceiling of the chamber.

Typically, we connected 13 panels to form the chamber arrangement shown in Fig. 1(b), enclosing a volume of $1.2\times1.2\times1.8$ m^2. A one-panel gap is left open in the middle side of the chamber as depicted, allowing samples the be easily moved in and out of the chamber. Note that during measurements, an absorber covered panel is placed over the opening. We also found it useful to partially connect a single panel at each end of the chamber with a simple hinge, allowing inspection and repositioning of the horn antennas if needed.

The chamber was placed on two long tables to position it at a convenient height. A gap is left between the tables to allow cables and horn antennas to reach into the chamber from underneath. This arrangement also allows the VNA to be placed directly under the middle of the chamber, minimizing the length of the cables needed to reach the horns. The VNA is then operated with a remote keyboard, mouse, and monitor, and/or via a network cable. Where possible, the table surface and gap are covered with absorber panels to absorb downward waves in the chamber.

C. Samples and Holder

Sample slabs should be as flat as possible to provide a nearly planar surface for reflection and transmission. In our results, we performed no special preparation of building material surfaces before performing measurements. In the case of stacks of bricks or blocks, we tried both block-staggered and block-aligned arrangements, trying to keep the front and back surfaces as flat as possible. Each sample was at least 60×60 cm^2 in facial area. Sample thickness depended on the material, but ranged from 2.2 mm (glass) to 58 mm (concrete block).

A wooden sample holder was built as depicted in Fig. 2, which can be used three different ways. For light samples, a single wooden board is placed in the holder, and samples are held to the board with clamps. For heavier samples, a 65×65 cm^2 rigid wooden frame was built that fits into the holder and allows the sample to be clamped securely on the top and sides. Third, for brick or block samples, a small wall of material is built by stacking bricks or blocks directly on top of the sample holder.

To avoid disturbing the chamber or antennas during measurements, we found it most convenient to use the following sequence:

1) Clamp the sample sheet to the frame outside of the chamber.
2) Place the frame in the holder inside the chamber.
3) Perform the S_{21} measurement with the VNA.
4) Remove the frame (and sample) from the sample holder and chamber, taking care not to bump the horn antennas.
5) Perform the S_{21} measurement for the air-only case with the VNA.

Likewise, for measurements involving stacks of bricks or blocks, the stack was built on the holder, the material measurement was performed, the stack was carefully removed, and then the air measurement was performed.

The need to not move antennas between the sample and air-only measurements is paramount for dependable and repeatable results. We found that placing the frame or stack in the chamber was more disruptive to the system than removing the sample, which is the reason for performing the air-only calibration measurement after the material measurement. Also, we found it important that the antenna tripods not touch or rest against the tables as they come through the gap. Shifting weight is placed on the tables when placing and removing samples, and this can move the antennas if their tripods are touching the tables.

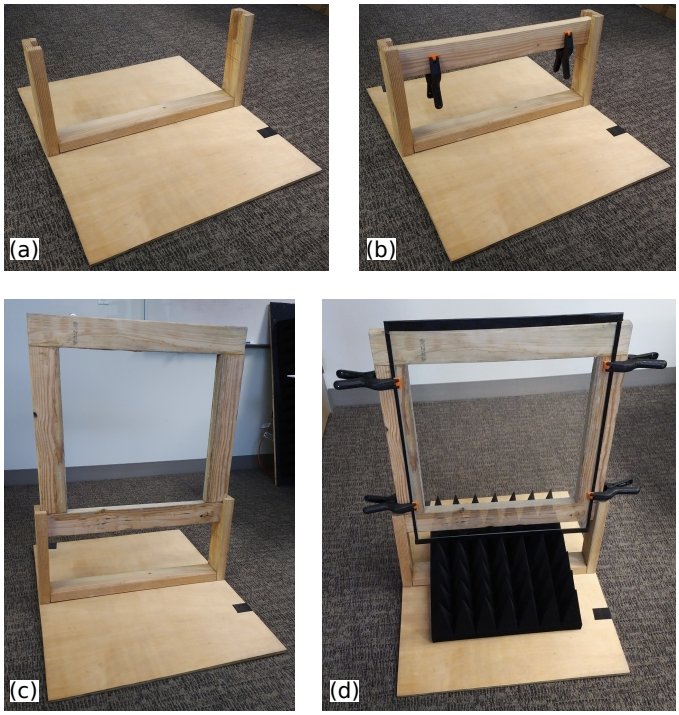

Fig. 2: Wooden fixture that was fabricated for holding material samples in the center of the chamber: (a) empty holder with slots, (b) holder with single cross board inserted for light samples clamped at the bottom, (c) holder with wooden frame inserted for heavier samples, and (d) frame configuration used in samples showing a clamped glass sample.

D. Antennas

Antennas covering the complete band of interest are needed to provide a seamless characterization of material properties. Ideally, antennas should have patterns that direct power to (or receive power from) the material surface without significant spillover at the material edges. These requirements are typically met by broadband horn antennas. Although lenses can be used to make wavefronts more planar at the material surface, the method we develop accounts for wavefront curvature, reducing the need for these components.

For our work, we used two RFSpin QRH40 4-40 GHz quad-ridged horns for transmit and receive. Although these horns support dual-polarization, in our measurements we only used a single port on each horn antenna (vertical polarization). Polarization dependence of some materials was checked by simply rotating the sample $90°$. In the future, we plan to use all four ports of the VNA and both antenna ports to allow automatic dual-polarization measurement of the samples. Antennas were connected to the VNA using 4-ft 2.92 mm cables (Fairview Microwave FMC2929914-48).

The beamwidth of the QRH40 antennas is largest at 4 GHz, where 3 dB beamwidth is approximately $90°$. The antenna apertures were placed approximately 40 cm away from the sample surface, which was chosen to provide an acceptable tradeoff between far-field distance considerations and the width of the illumination zone on the sample. Since a $90°$ beam is 80 cm wide at this distance[1], some spillover and edge diffraction is expected with 60-cm-wide samples, which is partially mitigated using a time-gating procedure. Beamwidth and illumination width drop with increasing frequency, and for most frequencies the sample is completely within the 3-dB antenna beamwidth. For example, at 8 GHz, the beamwidth is approximately $60°$, which means an illumination zone of 46 cm.

III. System Modeling

The goal of this section is to develop two basic models. The first model relates the transmission properties of the material slab in isolation to a practical S_{21} measurement, allowing a slab-only transmission coefficient S_{21}^{M} to be estimated. The second model provides a way to compute S_{21}^{M} as a function of the material complex permittivity ϵ_r, allowing the latter to be estimated from data.

A. System Two-Port Network Model

The purpose of this section is to develop a model relating measured S_{21} (which includes antennas and free-space propagation) to transmission properties of the slab alone. Note that although most quantities in this analysis depend on the excitation frequency f, we can assume f is fixed and drop the dependence when notationally convenient.

[1] $(40\ \mathrm{cm})(2)\tan(90°/2) = 80\ \mathrm{cm}$.

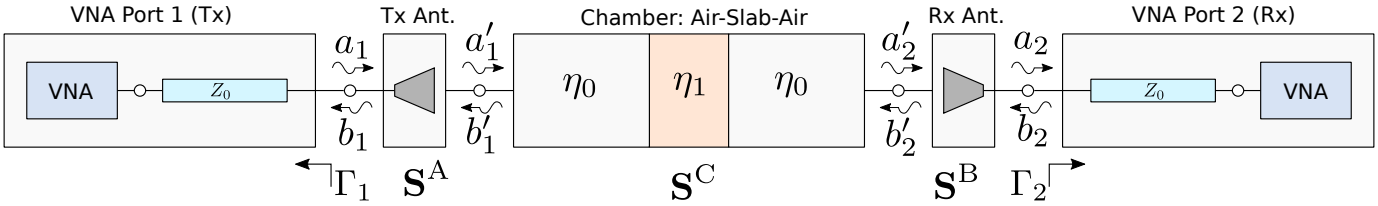

Fig. 3: S-parameter model of the material characterization setup shown in Fig. 1(a).

Perhaps the simplest representation of the system in Fig. 1(a) is the cascade of two-port network elements shown in Fig. 3. We assume a calibration has been performed of the VNA and cables, allowing these components to be lumped together. This calibration also ensures nearly zero reflection looking into the VNA cables, or $\Gamma_1 = \Gamma_2 = 0$. The transmit side of the system is characterized with S-parameters as

$$\begin{bmatrix} b_1 \\ a_1' \end{bmatrix} = \begin{bmatrix} S_{11}^{\mathrm{A}} & S_{12}^{\mathrm{A}} \\ S_{21}^{\mathrm{A}} & S_{22}^{\mathrm{A}} \end{bmatrix} \begin{bmatrix} a_1 \\ b_1' \end{bmatrix}, \tag{2}$$

which relates the incident wave radiated by the Tx antenna (a_1') to the forward wave launched by the VNA (a_1) and the reflected wave from the slab (b_1'). Reflections from the slab (b_1') are mostly absorbed by the chamber walls, received by the antenna, or otherwise time-gated out, meaning we can treat $S_{22}^{\mathrm{A}} \approx 0$, and in this case

$$a_1' = S_{21}^{\mathrm{A}} a_1. \tag{3}$$

At the receive side, we have the relationship

$$\begin{bmatrix} b_2' \\ a_2 \end{bmatrix} = \begin{bmatrix} S_{11}^{\mathrm{B}} & S_{12}^{\mathrm{B}} \\ S_{21}^{\mathrm{B}} & S_{22}^{\mathrm{B}} \end{bmatrix} \begin{bmatrix} a_2' \\ b_2 \end{bmatrix}. \tag{4}$$

Assuming that the transmitted wave is absorbed in the chamber walls, received by the antenna, or otherwise time-gated out, we have $S_{11}^{B} \approx 0$. Further, reflection looking into the calibrated VNA is $\Gamma_2 = 0$, meaning $b_2 = 0$ and therefore $b_2' = 0$. This results in the simple expression

$$a_2 = S_{21}^{\mathrm{B}} a_2'. \tag{5}$$

The center of the chamber, which consists of an air region surrounding a material slab, can also be characterized by 2-port S-parameters, or

$$\begin{bmatrix} b_1' \\ a_2' \end{bmatrix} = \begin{bmatrix} S_{11}^{\mathrm{C}} & S_{12}^{\mathrm{C}} \\ S_{21}^{\mathrm{C}} & S_{22}^{\mathrm{C}} \end{bmatrix} \begin{bmatrix} a_1' \\ b_2' \end{bmatrix}, \tag{6}$$

and since there can be multiple reflections and transmissions inside of the slab, all S-parameters here are nonzero in general. Since we have $b_2' = 0$ from previous assumptions, we can write

$$a_2' = S_{21}^{\mathrm{C}} a_1'. \tag{7}$$

Combining (3), (5), and (7), we have

$$a_2 = S_{21}^{\mathrm{B}} S_{21}^{\mathrm{C}} S_{21}^{\mathrm{A}} a_1. \tag{8}$$

Thus, our VNA S_{21} measurement should give approximately

$$S_{21}(f) = S_{21}^{\mathrm{B}}(f) S_{21}^{\mathrm{C}}(f) S_{21}^{\mathrm{A}}(f). \tag{9}$$

The terms S_{21}^{B} and S_{21}^{A} can be very complicated to model, since they will depend on detailed antenna properties, placement of the antennas, etc. We therefore use a measurement of an air sample with known S_{21}^{C} to approximately remove S_{21}^{B} and S_{21}^{A} without explicitly knowing them.

Considering the geometrical arrangement of antennas and material slab in Fig. 4, we can model $S_{21}(f)$ according to propagation from the Tx antenna to the left slab surface, multiple reflections inside the slab, and propagation from the right slab surface to the Rx antenna. Mathematically, we have

$$S_{21}(f) = \underbrace{S_{21}^{\mathrm{A}}(f) \frac{\exp(-jk_0 D)}{\sqrt{A_0} D^{\gamma}}}_{\text{Tx to Slab}} \underbrace{\sum_{n=0}^{\infty} p_n(f) \left[\frac{D}{D + D' + (2n+1)d}\right]^{\gamma}}_{\text{Inside Slab}} \underbrace{S_{21}^{\mathrm{B}}(f) \exp(-jk_0 D')}_{\text{Slab to Rx}}, \tag{10}$$

$$= S_{21}^{\mathrm{A}}(f) S_{21}^{\mathrm{B}}(f) \frac{\exp[-jk_0(D + D')]}{\sqrt{A_0}} \sum_{n=0}^{\infty} p_n(f) \left[D + D' + (2n+1)d\right]^{-\gamma}, \tag{11}$$

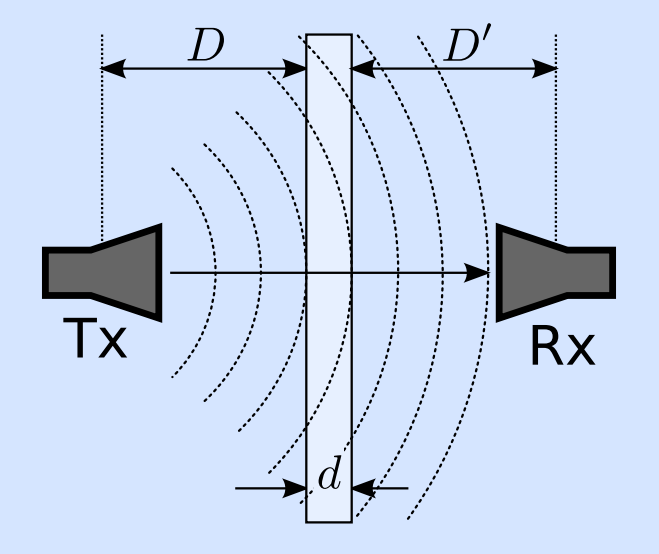

Fig. 4: Arrangement of transmit (Tx) and receive (Rx) antennas, where the material slab occupies a region of thickness d. Distances D and D' are measured from the Tx antenna phase center to the slab surface and from the slab surface to the Rx antenna phase center, respectively.

where $k_0 = 2\pi f/c_0$ is the wavenumber, c_0 is the speed of light in vacuum, and $\gamma = 0,\ 0.5,$ or 1 for planar (1D), cylindrical (2D), or spherical (3D) waves, respectively. The constant A_0 is the area of a unit surface, defined to be $1,\ 2\pi,$ or 4π for 1D, 2D, or 3D waves. The sum represents the contribution from multiple reflections inside the slab, where $p_n(f)$ gives the complex amplitude (ignoring wave spreading) of the nth partial wave emerging from the right slab boundary. The bracketed term in the sum captures effective attenuation due to wave spreading as a wave propagates from the left slab boundary, experiences n reflections inside the slab, emerges from the slab at the right boundary, and propagates to the Rx antenna.

When the material slab is replaced with air, only a single partial wave propagates from Tx to Rx with $p_0(f) = \exp(-jk_0 d)$, and we have

$$S_{21}^{\mathrm{M(air)}} = S_{21}^{\mathrm{A}}(f) S_{21}^{\mathrm{B}}(f) \frac{\exp[-jk_0(D+D')]}{\sqrt{A_0}} \exp(-jk_0 d) \left[D + D' + d\right]^{-\gamma}. \tag{12}$$

Comparing (11) and (12) suggests we calibrate each material measurement using

$$S_{21}^{\mathrm{M}}(f) = \frac{S_{21}(f)}{S_{21}^{\mathrm{air}}(f)\exp(jk_0 d)} \left[\frac{D+D'}{D+D'+d}\right]^{\gamma} \triangleq S_{21,\mathrm{msmt}}^{\mathrm{M}}(f) \tag{13}$$

$$= \sum_{n=0}^{\infty} p_n(f) \left[1 + (2n+1)\frac{d}{D+D'}\right]^{-\gamma}, \tag{14}$$

where $S_{21}^{\mathrm{M}}(f)$ represents propagation in the slab, taking into account effective attenuation due to wave spreading in excess of the air-only case. To complete the model, we need to find the $p_n(f)$, which are the complex amplitudes of the partial waves that exit from the right slab boundary given unit incident field amplitude on the left boundary.

B. Slab Transmission Model

In this section we derive the $p_n(f)$ required for S_{21}^{M}, resulting in a model that takes into account absorption, propagation, and wave spreading in a homogeneous slab. Consider the arrangement in Fig. 5. The slab with complex permittivity $\epsilon_r = \epsilon_r' - j\epsilon_r''$ and intrinsic impedance $\eta_1 = \eta_0/\sqrt{\epsilon_r}$ is surrounded by air with intrinsic impedance $\eta_0 = 376.7\ \Omega$. We let $a(x)$ be the forward wave complex amplitude (electric field intensity) at distance x, for unit incident amplitude on the left face of the slab, or $a(0^-) = 1$. A wave traveling from air into the slab experiences reflection coefficient

$$\Gamma_0 = \frac{\eta_1 - \eta_0}{\eta_1 + \eta_0} \tag{15}$$

and transmission coefficient $1 + \Gamma_0$. Likewise a wave traveling from the slab into air experiences reflection coefficient $\Gamma_1 = -\Gamma_0$ and transmission coefficient $1 - \Gamma_0$. The one-way complex transmission coefficient for a single traversal of the slab is

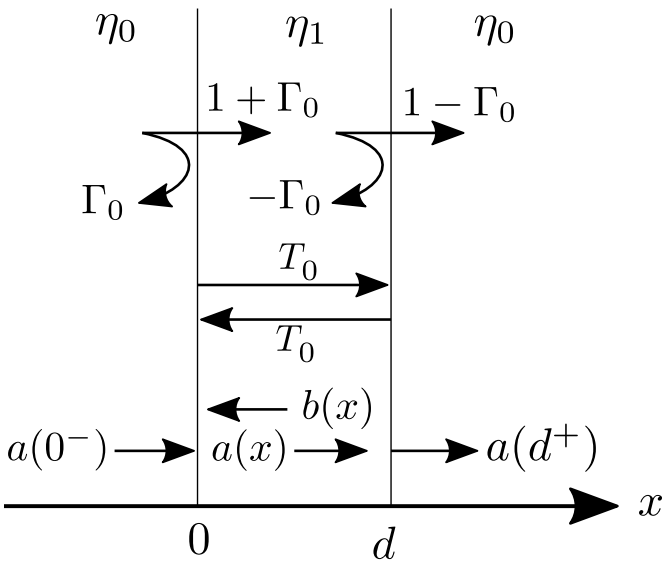

Fig. 5: Quantities needed to derive S_{21}^{M}, the S-parameter model of the slab section.

$T_0 = \exp(-jk_1 d)$, which accounts for both attenuation of the wave amplitude and its change in phase. The total complex amplitude emerging from the right face can be written as

$$a(d^+) = (1-\Gamma_0)a(d^-) \tag{16}$$

$$= (1-\Gamma_0)\sum_{n=0}^{\infty} a_n(d^-), \tag{17}$$

where $a_n(x)$ denotes the complex wave amplitude due to the nth partial reflection in the medium. Specifically, $n=0$ represents the direct path through the medium, $n=1$ is the first reflection, etc. The zeroth reflection term is found as

$$a_0(d^-) = a_0(0^+)T_0 \tag{18}$$

$$= (1+\Gamma_0)T_0. \tag{19}$$

The first reflection is found by following the zeroth reflection as it reflects at $x=d$, travels back and reflects at $x=0$ and then travels again to $x=d$, or

$$a_1(d^-) = a_0(d^-)(-\Gamma_0)T_0(-\Gamma_0)T_0 \tag{20}$$

$$= a_0(d^-)\Gamma_0^2 T_0^2. \tag{21}$$

Continuing this procedure, the wave amplitude due to the nth reflection is found as

$$a_n(d^-) = \begin{cases} (1+\Gamma_0)T_0, & n=0, \\ \Gamma_0^2 T_0^2 a_{n-1}(d^-), & \text{otherwise.} \end{cases} \tag{22}$$

Recognizing that $p_n(f) = a_n(d^+) = (1-\Gamma_0)a_n(d^-)$, we have

$$S_{21}^{\mathrm{M}}(f) = (1-\Gamma_0)\sum_{n=0}^{\infty} a_n(d^-)\left[1+(2n+1)\frac{d}{D+D'}\right]^{-\gamma} \triangleq S_{21,\mathrm{mod}}^{\mathrm{M}}(f). \tag{23}$$

Although the sum is technically infinite, in practice only a few terms need to be computed (no more than 10) for good convergence.

C. Time-gate Filtering

Although having an anechoic enclosure for the measurement system ensures that most unwanted waves are absorbed, diffraction from material sample edges and scattering from antennas and fixtures can distort the signal of interest. Fortunately, most of these effects arrive at the receive antenna much later than the desired signal, and time-gating can be used to improve signal fidelity.

Parameters of an appropriate time window are found by inspection of the air-only measurement, since this indicates the shortest delay that should be expected. To this end, $S_{21}^{\mathrm{air}}(f)$ is multiplied by a Blackman window and transformed to the time domain with an FFT to obtain $S_{21}^{\mathrm{air}}(t)$, where an example is plotted in Fig. 6. The time-gate window is specified as the temporal

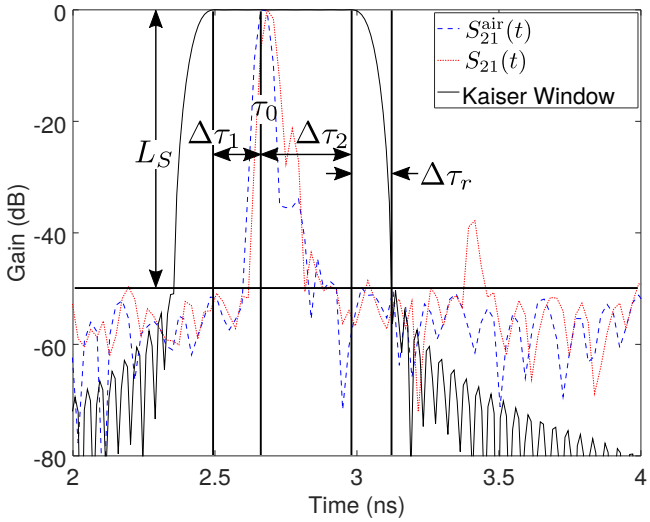

Fig. 6: Example of a time window specification for time-gating operation. The center of the window is at τ_0, corresponding to the peak of the air-only measurement. The window size is set by $\Delta\tau_1$ and $\Delta\tau_2$, and rolloff time by $\Delta\tau_r$. The parameter L_S is stop-band attenuation.

TABLE I: Kaiser Window Parameters

Thickness	2.5 mm	7.5 mm	25 mm	50 mm
$\Delta\tau_1$	5 ns			
$\Delta\tau_2$	10 ns	10 ns	30 ns	60 ns
$\Delta\tau_r$	4 ns			
L_S	50 dB			
R_P	0.1 dB			

span $\Delta\tau_1$ and $\Delta\tau_2$ before and after the peak response delay τ_0, respectively. Although a fixed value for $\Delta\tau_1$ can be used, the value of $\Delta\tau_2$ should depend on the sample thickness and number of reflections in the sample that should be retained.

In this work we have used the popular Kaiser window, which is specified in terms of the start ($\tau_0 - \Delta\tau_1$) and stop ($\tau_0 + \Delta\tau_2$) times, roll-off time $\Delta\tau_r$, pass-band ripple R_P, and stop-band attenuation L_S. Table I shows the parameters that we have used for the Kaiser window for various material thicknesses. Once computed, the Kaiser time window $w(t)$ is transformed to the frequency domain to obtain $W(f)$. Time-gated versions of the frequency-domain signals for air ($S_{21}^{\text{air}}(f)$) and material ($S_{21}(f)$) are obtained with

$$S_{21}^{\text{air}\prime}(f) = S_{21}^{\text{air}}(f) * W(f) \tag{24}$$

$$S'_{21}(f) = S_{21}(f) * W(f), \tag{25}$$

where $*$ represents convolution. These time-gated versions (the primed quantities) are then used instead of the raw values in the method developed previously.

A known problem with time-gating is significant distortion of signals at frequencies near the high and low limits of the frequency-domain measurement. A recent method for mitigating these effects appeared in [3], which is adopted in this work. The idea is to apply linear prediction at the frequency domain boundaries to extend the measurement slightly outside of the original measurement span. After filtering (convolving) this lengthened signal with $W(f)$, the signal is again clipped back to the original frequency boundaries. Simulations of an idealized measurement setup show that this procedure provides useful reduction of distortion at the band edges.

D. GPU-Based Estimation Procedure

The results in the previous sections may now be used to estimate ϵ_r from a free-space measurement of the material slab ($S_{21}(f)$), followed by an air-only measurement (S_{21}^{air}). The basic approach is to search for $\epsilon_r(f)$ that minimizes the error of measured (13) and modeled (23) transmission in a least-squares sense, or

$$\epsilon_{\text{r,opt}} = \arg\min_{\epsilon_r(f)} \sum_n \left| S_{21,\text{msmt}}^{\text{M}}(f_n) - S_{21,\text{mod}}^{\text{M}}(f_n, \epsilon_r(f_n)) \right|^2, \tag{26}$$

where f_n is the nth VNA frequency sample. To avoid only finding locally optimal solutions, we use a direct sampling-based search procedure, outlined below.

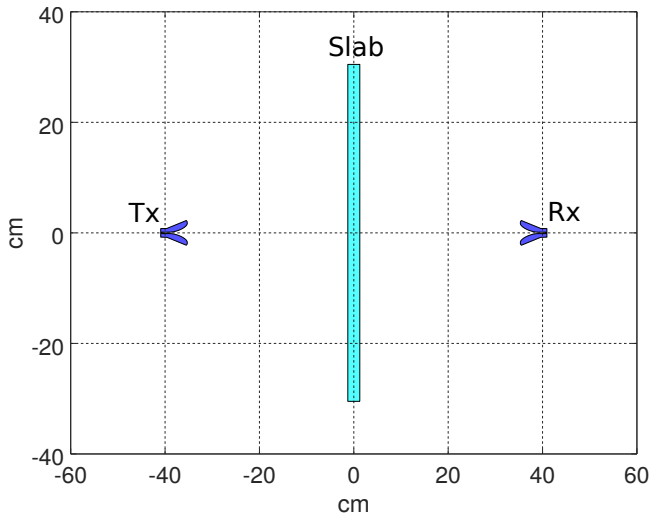

Fig. 7: Two-dimensional (2D) model used for method-of-moments (MOM) simulations. Transmit (Tx) and receive (Rx) ridged horns are simulated with perfect-electrical conductors, and the slab is a box with arbitrary complex permittivity and thickness.

It is expected that ϵ_r will change gradually with frequency, and some type of regularization or model should be applied to improve the fitting results. One option is to assume a physical model, such as the Debye or Cole-Cole [4] models, where the search is performed over the parameters of those models. One problem with this approach is that the large number of parameters may result in a very long search. We have instead taken an unstructured approach that assumes piecewise linear variation of ϵ_r in a number of frequency bands. A fast GPU-based code is used to compare measured and modeled S_{21}^{M} over all possible values of ϵ_r in each band for a specified range and resolution on the real and imaginary parts of ϵ_r. Although we envision future enhancements to the GPU-based code, we document the basic operation of our current implementation here. Since it is difficult to provide all details of the implementation, only the basic operation will be described, with complete source code available online [5] for interested readers.

The algorithm works by first assuming constant permittivity over the whole measurement sweep, and searching for the best fit of measured and modeled S_{21}^{M} over all possible values of ϵ_r' and ϵ_r'' sampled to a given precision. We typically use the ranges of $\epsilon_r' \in [1, 15]$ and $\epsilon_r'' \in [0, 2]$, sampled at a resolution of 0.01. This results in $N_{\epsilon_r'} = 1401$ and $N_{\epsilon_r''} = 201$ search points in each dimension. Note that (26) can be computed for the required $N_{\epsilon_r'} N_{\epsilon_r''} = 2.8{\times}10^5$ points in less than one second on the RTX-2060 GPU we are using.

In the next step, the data is divided into N_{band} frequency bands, where band endpoints are denoted F_n with $n = 1, \ldots, N_{\mathrm{band}} + 1$, and piecewise linear variation of ϵ_r is assumed in each band. The code implements an iterative procedure to optimize $\epsilon_r(F_n)$, which consists of M outer iterations with $N_{\mathrm{band}} + 1$ inner iterations each. The nth inner iteration only considers the effect of $\epsilon_r(F_n)$ on the fit, computing (26) for all $N_{\epsilon_r'} N_{\epsilon_r''}$ possible values of $\epsilon_r(F_n)$, where the value giving the best fit is kept for the next iteration.

Although the computational complexity of the direct search procedure is high, it can be performed very quickly on the GPU. As an example, for $M = 5$ outer iterations, $N_{\mathrm{band}} = 6$, $N_{\epsilon_r'} = 1401$, $N_{\epsilon_r'} = 201$, and 1001 VNA frequency points, the complete GPU-based search procedure only requires 2.1 seconds on the RTX-2060.

IV. Method-of-Moments (MOM) Based Validation

In order to understand the accuracy and possible limitations of the free-space measurement approach, it is desirable to apply the method to materials with known properties. For example, in Section V we perform a measurement of Teflon, which is a well characterized material in microwave bands. Unfortunately, there are only a few such well-characterized materials. Also, even well-characterized materials exhibit variation in their complex permittivity due to manufacturing variations, temperature changes, etc. In this section, we explore the validity of the developed method taking a numerical electromagnetics approach, allowing the complex permittivity of the simulated sample to be exactly specified and known.

One problem with simulating the measurement setup is that the chamber is electrically large. The chamber dimensions are $1.22 \times 1.22 \times 1.83$ m^3, which at 40 GHz ($\lambda = 7.5$ mm wavelength) is $160 \times 160 \times 240$ λ^3, which is too large to be easily simulated with standard solvers on a conventional PC. The main effects that should be simulated are wave curvature (near-field effects) and diffraction at the sample edges, and these effects will also be present in a 2D simulation of the setup. Therefore, to allow simulations to proceed given existing computational limitations, we have utilized a 2D model of the scenario, as depicted in Fig. 7. The main difference is that we should expect cylindrical (2D) wave spreading, as opposed to the spherical (3D) spreading in the actual chamber.

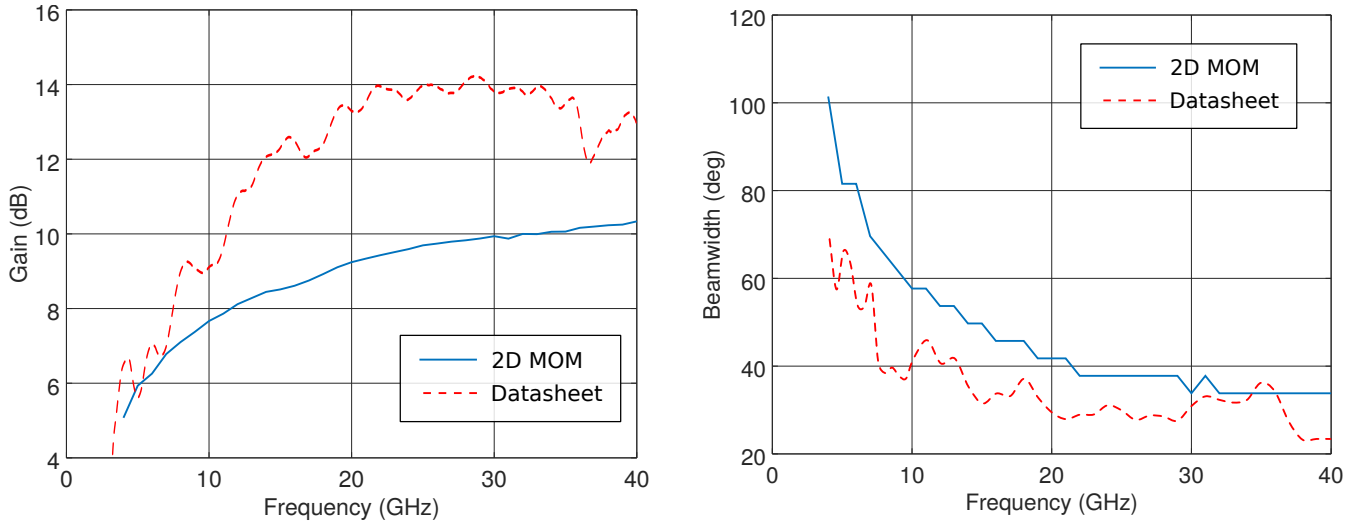

(a) Gain

(b) 3 dB Beamwidth

Fig. 8: Gain (a) and 3 dB beamwidth (b) of double-ridged horn as simulated with 2D MOM, compared with typical curves given on SpinRF QRH-40 datasheet.

Given our past background with finite-difference time-domain (FDTD) simulations, our first approach was to apply an FDTD solver for the 2D chamber. Initial simulations were very promising, allowing a broadband 4-40 GHz simulation of the chamber to be performed with a single FDTD simulation in about 30 minutes, which only utilized a single PC core. One problem we faced, however, is that our FDTD code only supports a constant material conductivity, which led to very high and very low ϵ_r'' at low and high frequencies, respectively. Not only was the steep slope of ϵ_r'' unrealistic, it hampered statistical analysis of the error. A possible solution is to implement dispersive materials, such as the Debye model, and fit the model parameters to simulate a flatter ϵ_r'' profile [6], but significant time and testing would be required to extend the FDTD code. A second problem we encountered was unwanted numerical dispersion of propagating waves at high frequencies due to the very large domain. Although this could also be corrected [7], we decided to search for another method.

An alternative approach was found by utilizing the 2D method-of-moments (MOM) technique that was developed previously for body-area-network simulations [8]. The code that was developed for [8] is a frequency-domain solver that simulates a 2D slab with arbitrary shape and complex permittivity. A very simple extension of the method and code provides a way to simulate metal surfaces, allowing 2D ridged horns to be efficiently modeled. Simulated data is produced with the MOM code by running a simulation for each of 401 sample points over the 4 to 40 GHz range. We point out that our MATLAB MOM implementation is much slower than our binary C/C++ FDTD solver. Approximately 3 minutes are required for each frequency point with MOM, totaling about a day of processing time for a full 401-point sweep. Running jobs in parallel on a multi-core PC, we were able to analyze 28 different materials in about one week of processing time.

We first simulated a 2D double-ridged horn antenna with MOM to ensure correct operation over our band of interest. Although we do not have an exact model for the QRH-40 horn antenna, the ridge shape is apparent with a visual inspection. The same shape was captured in the computer by taking a close-up photo of the antenna, importing that image into Inkscape, and drawing over the top of the image to create a vectorized model. We fed the antenna by simply terminating the back of the ridge structure with a short circuit (metal wall) and placing a vertically oriented point current slightly to the right of the wall.

Fig. 8 shows simulated gain and 3-dB beamwidth in the vertical plane (E-plane) of the MOM simulated horn, showing somewhat lower gain and higher beamwidth than published values on the QRH-40 datasheet. These differences should be expected, given that the actual 3D antenna is an enclosed quad-ridged horn, whereas only a double-ridged structure can be simulated in 2D. In light of this comparison, we expect material characterization with the simulated 2D horns to be more challenging than with the actual horn antennas, since larger simulated beamwidth means more spillover at the material edges.

Simulation of the receive horn required some type of load to be placed at the back of the horn. This was accomplished by implementing an impedance surface element, allowing waves normal to the element to be mostly absorbed. Figs. 9(a) and (b) show fields around the transmit horn and receive horn, respectively at 20 GHz. The layout of our complete system model is depicted in Fig. 7, consisting of the transmit horn (left), material slab (center), and receive horn (right). The code is a boundary-element (surface-based) method, where the metal and lossy material outer boundaries are meshed (segmented) at a specified resolution. We chose a mesh density of 20 segments per wavelength at the highest frequency (40 GHz).

Fig. 10 shows fields in the simulation domain due to radiation from the left horn and scattering from the slab, which represents the incident field for the right horn. The example simulation shown was performed at 5 GHz with $\epsilon_r = 3 - j0.1$

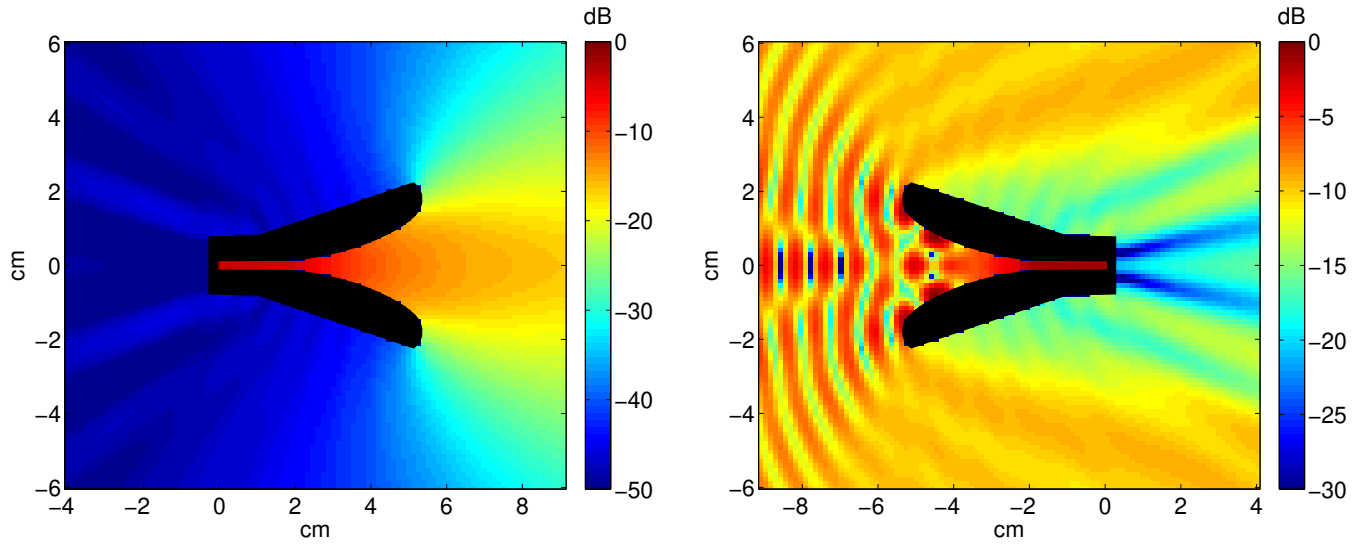

(a) Transmit (b) Receive

Fig. 9: MOM simulations of the (a) transmit and (b) receive horns at 20 GHz.

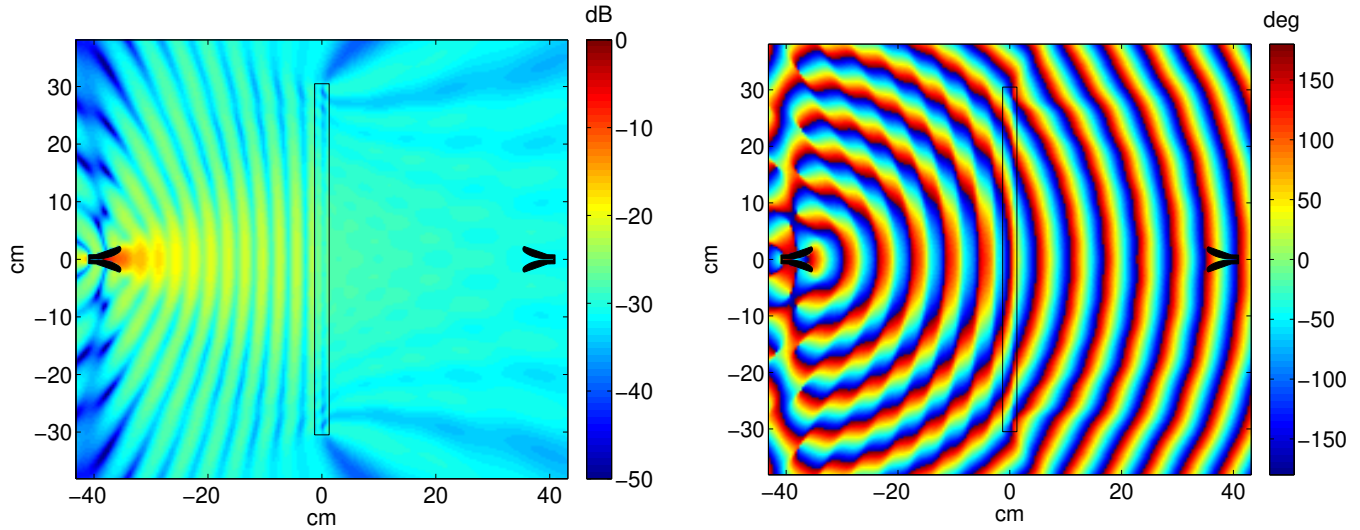

(a) Amplitude (b) Phase

Fig. 10: MOM simulation of the chamber simulation domain, not including scattering due to the receive horn antenna (right). Amplitude (a) and phase (b) of the H_z field component are plotted for an excitation frequency of 5 GHz with $\epsilon_r = 3 - j0.1$ and $d = 25$ mm.

and $d = 25$ mm. Although some scattering effects are seen due to edges of the sample, field amplitude in the vicinity of the receive antenna is fairly uniform. Also, the phase plot reveals that incident field wave fronts are nearly cylindrical near the receive horn.

The MOM code was used to analyze all 27 combinations of $\epsilon_r' \in \{1.1, 3.0, 10.0\}$, $\epsilon_r'' \in \{0.01, 0.1, 1.0\}$, and $d \in \{2.5, 7.5, 25\}$ mm, as well as an air-only measurement. The developed method was first applied to the simulated data without any extra noise being added, which is denoted the infinite SNR case. Next, for each simulated material sample, 100 random frequency-domain noise-corrupted realizations were generated, and complex permittivity was estimated from this data for SNRs of 20 and 30 dB. Note that the relatively high SNR considered here is consistent with controlled measurement in a compact chamber. A given SNR level is realized by computing the noise variance according to

$$\sigma^2_{\text{Noise}}(f) = |S_{21}(f)|^2 10^{-\frac{\text{SNR}_{\text{dB}}}{10}}, \tag{27}$$

TABLE II: Percent RMS Error in ϵ_r'

SNR	20 dB			30 dB			∞		
d (mm) / ϵ_r	2.5	7.5	25	2.5	7.5	25	2.5	7.5	25
1.1 - 0.01j	5.6	2.0	0.6	1.7	0.7	0.2	0.0	0.0	0.0
3.0 - 0.01j	2.7	1.3	0.4	1.0	0.5	0.2	0.4	0.3	0.3
10.0 - 0.01j	1.9	0.6	0.4	0.9	0.3	0.3	0.6	0.2	0.3
1.1 - 0.10j	4.6	2.2	0.6	1.9	0.7	0.2	0.0	0.0	0.0
3.0 - 0.10j	2.9	1.4	0.4	0.9	0.5	0.2	0.4	0.3	0.3
10.0 - 0.10j	1.7	0.6	0.4	0.8	0.3	0.3	0.6	0.2	0.3
1.1 - 1.00j	5.6	2.8	327.7	2.3	1.0	285.1	0.0	0.3	282.9
3.0 - 1.00j	3.4	1.3	30.0	1.1	0.5	1.5	0.4	0.4	1.4
10.0 - 1.00j	1.8	0.7	0.6	0.8	0.3	0.5	0.6	0.2	0.5
Mean	1.9 (σ=1.6)			0.8 (σ=0.6)			0.3 (σ=0.3)		

TABLE III: Absolute RMS Error in ϵ_r''

SNR	20 dB			30 dB			∞		
d (mm) / ϵ_r	2.5	7.5	25	2.5	7.5	25	2.5	7.5	25
1.1 - 0.01j	0.04	0.02	0.01	0.01	0.01	0.00	0.00	0.00	0.00
3.0 - 0.01j	0.04	0.02	0.01	0.02	0.01	0.01	0.01	0.00	0.01
10.0 - 0.01j	0.12	0.03	0.03	0.05	0.01	0.03	0.03	0.01	0.03
1.1 - 0.10j	0.06	0.02	0.01	0.02	0.01	0.00	0.00	0.00	0.00
3.0 - 0.10j	0.07	0.04	0.01	0.02	0.01	0.01	0.01	0.00	0.01
10.0 - 0.10j	0.13	0.05	0.03	0.06	0.02	0.02	0.04	0.01	0.03
1.1 - 1.00j	0.09	0.03	0.28	0.03	0.01	0.25	0.01	0.01	0.25
3.0 - 1.00j	0.10	0.04	0.09	0.03	0.01	0.05	0.01	0.01	0.05
10.0 - 1.00j	0.18	0.06	0.02	0.07	0.03	0.02	0.03	0.01	0.02
Mean	0.05 (σ=0.04)			0.02 (σ=0.02)			0.01 (σ=0.01)		

and each noise-corrupted realization is generated as

$$S_{21,\text{Noisy}}(f) = S_{21}(f) + \mathcal{CN}(0, \sigma^2_{\text{Noise}}(f)), \tag{28}$$

where $\mathcal{CN}(0, \sigma^2)$ denotes a zero-mean complex Gaussian distribution with total complex variance σ^2.

Figure 11 shows the fit of ϵ_r for the a simulated material with $\epsilon_r = 3 - j0.1$ and thickness 7.5 mm. For this middle case, a good fit and relatively low error in complex permittivity are obtained. Figure 12 shows a more challenging estimation case with $\epsilon_r = 1.1 - j1.0$ and thickness 25 mm, where the estimation procedure clearly fails at high frequency, which is due to virtually zero signal power penetrating the material.

The percent RMS error of estimated ϵ_r' is given in Table II, where estimation cases considered as "failed" (25% error or more) are marked in red. We observe that for moderate SNR (20 dB), error in ϵ_r' is 6% or better for cases that were not marked as "failed." Average error for non-failed cases (and error standard deviation σ) is given at the bottom of the table for each SNR. The failed cases represent thick samples with high loss and lower permittivity. Although somewhat alarming, it should be noted that high loss and low permittivity are usually not seen in realistic building materials. If such materials are encountered, they are more appropriately analyzed using other techniques, such as open-ended coaxial probes [9], [10] or open resonators [11].

Table III lists estimation error in the loss term ϵ_r'' for the same simulated cases. Since ϵ_r'' is very low for some cases, it is not meaningful to represent error as a percent, and absolute RMS error values are given instead. Note that estimation of ϵ_r'' fails for the same cases as ϵ_r' (maximum error set at 0.2), and estimation error is clearly higher for thinner samples and for samples with high permittivity. For the non-failed cases, average error in ϵ_r'' is about ± 0.05 for moderate SNR (20 dB), which translates into a loss tangent of approximately ± 0.01.

We conclude this section by summarizing that simulations confirm that the estimation procedure provides reasonable accuracy for the cases of practical interest. Error in the ϵ_r' is approximately 6% or lower, and error in loss tangent is about $\pm$ 0.01.

V. Sample Measurements

This section presents the results of material measurements using the methods described in previous sections. The thickness of each sample was estimated by measuring the thickness of each edge (at the center) with a digital caliper and computing the average. Repeatability of measurements was checked by performing five measurement cycles for most of the materials, where a measurement cycle consists of placing the sample in the chamber, measuring $S_{21}(f)$, removing the sample, and measuring the air-only $S_{21}^{\text{air}}(f)$. For brick or block samples (red brick, concrete brick, concrete slab), the block wall was rebuilt each time, which is likely to create more variation than that seen for a single sheet or slab.

In the sections below, we treat each of the materials that was measured in this study. In addition to estimating and plotting the complex permittivity of each sample, we compute and plot the best linear fit of ϵ_r' and ϵ_r''. Dielectric resonator measurements were presented in [12] as a way of validating real permittivity in the lower band, and these are also plotted where appropriate.

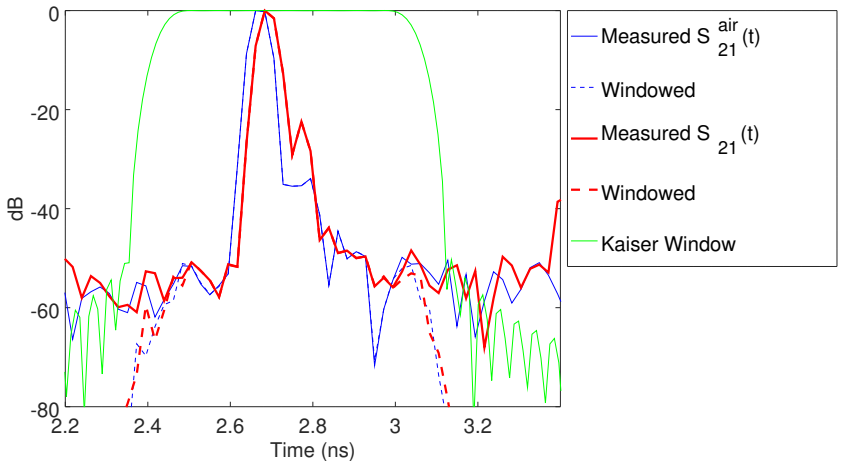

(a)

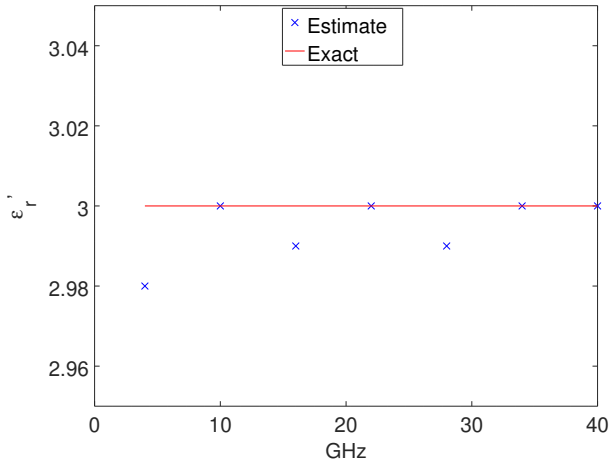

(b)

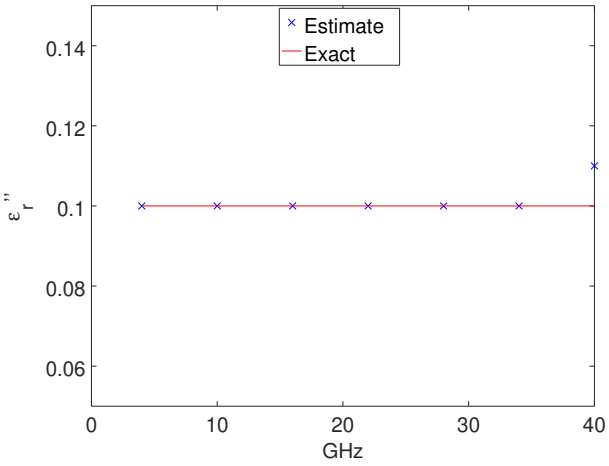

(c)

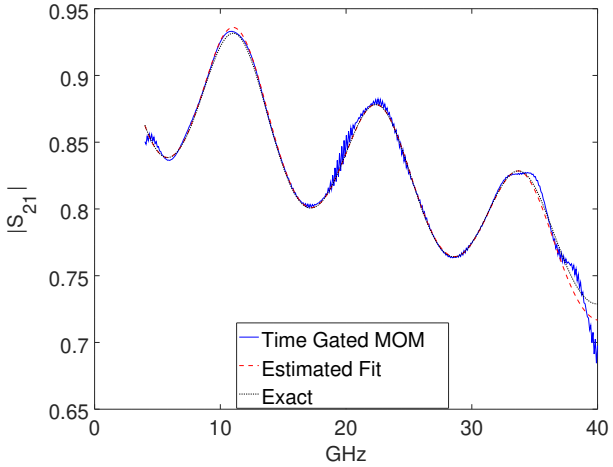

(d)

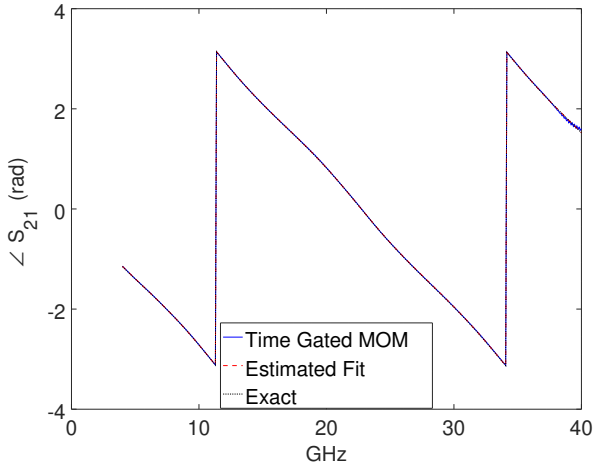

(e)

Fig. 11: Complex permittivity estimation for a simulated material sample with $\epsilon_r = 3 - j0.1$ and $d = 7.5$ mm: (a) time-gating procedure, (b) estimated ϵ_r', (c) estimated ϵ_r'', and the resulting fit of $S_{21}^{\mathrm{M}}(f)$ in terms of (d) magnitude and (e) phase.

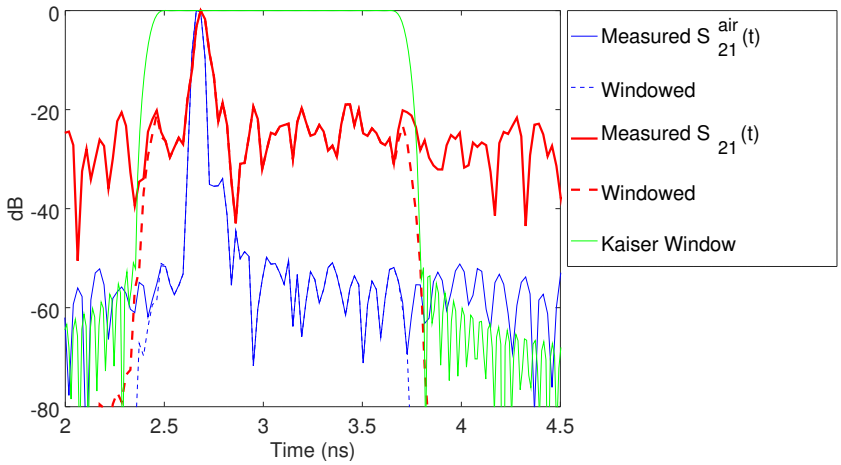

(a)

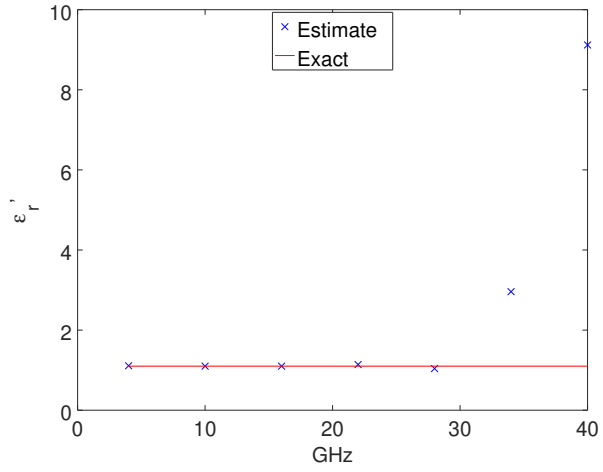

(b)

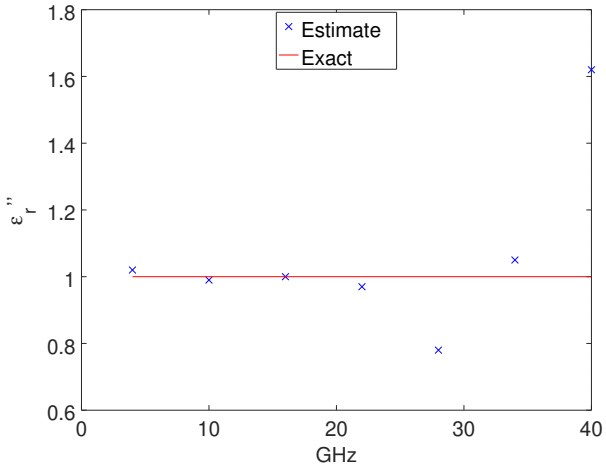

(c)

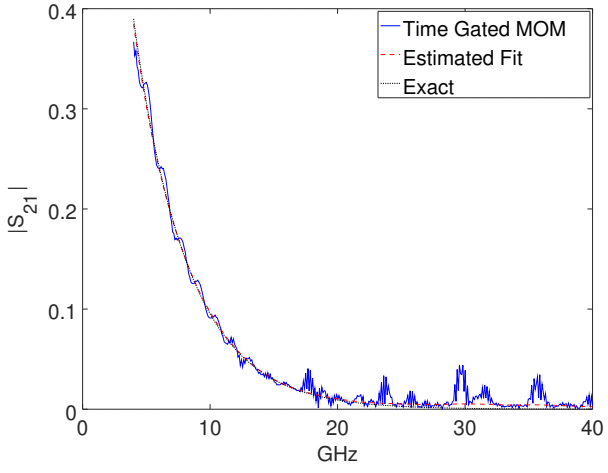

(d)

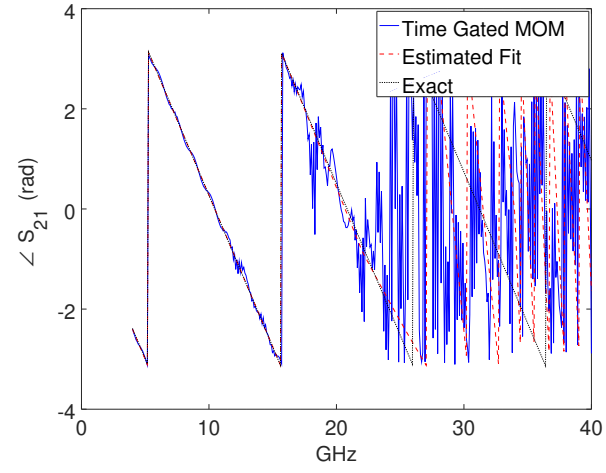

(e)

Fig. 12: Complex permittivity estimation for a simulated material sample with $\epsilon_r = 1.1 - j1.0$ and $d = 25$ mm: (a) time-gating procedure, (b) estimated ϵ_r', (c) estimated ϵ_r'', and the resulting fit of $S_{21}^{\mathrm{M}}(f)$ in terms of (d) magnitude and (e) phase.

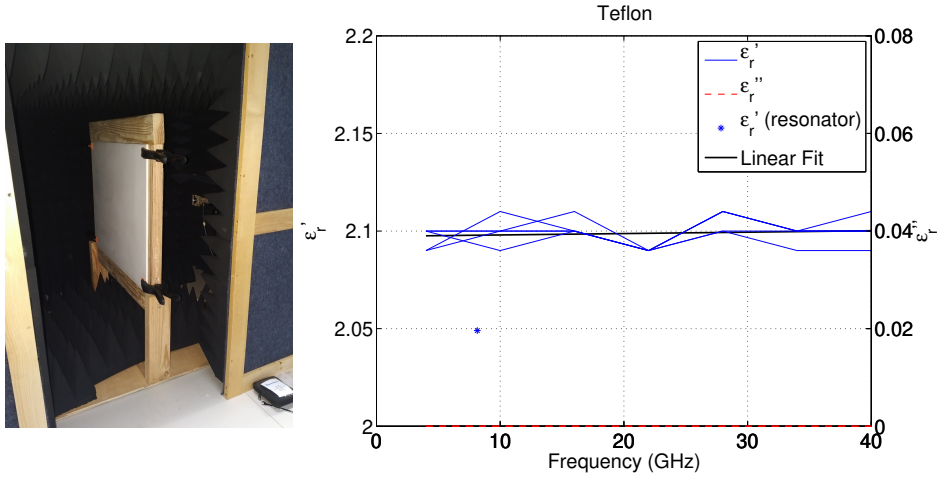

Fig. 13: Extracted complex permittivity of Teflon.

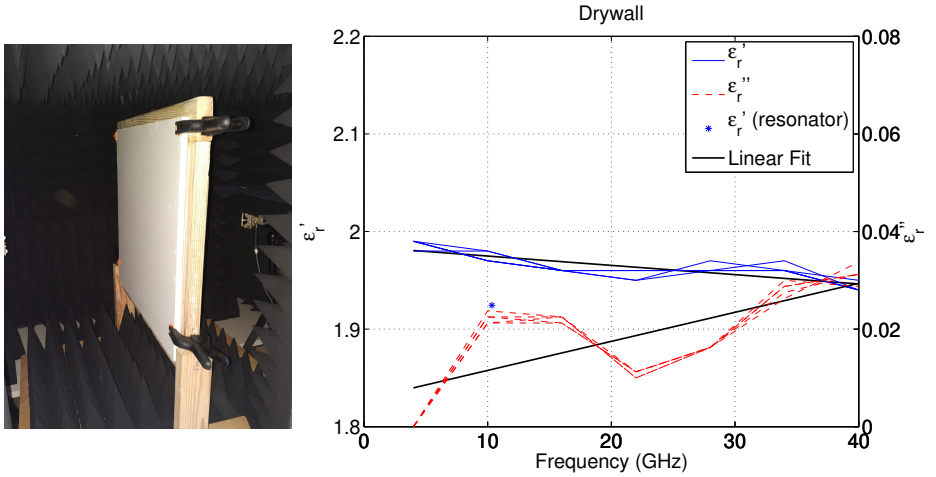

Fig. 14: Extracted complex permittivity of drywall.

A. *Teflon (PTFE)*

Given its well known characteristics in microwave bands, Teflon was chosen as the first test material in this study. The typical accepted value of real permittivity for Teflon (PTFE) is 2.1. Loss tangent varies somewhat with frequency, but is typically lower than 0.001, which for the purpose of our measurement technique is basically lossless. For a recent comprehensive measurement study of Teflon, see [13], which gives a value of $\epsilon_r \approx 2.03$ and loss tangent 0.0003 over the 4-40 GHz range. We used the Teflon sheet depicted in Fig. 13 having a thickness of 7.22 mm.

Fig. 13 plots the fitted permittivity of Teflon. The estimation code selects zero loss ($\epsilon_r'' = 0$) for all five repeated measurements over the complete frequency range. Estimated ϵ_r' is highly clustered around a value of 2.10.

B. *Drywall*

Drywall is a very common material used for the surface of interior walls in the U.S. The material sample with thickness $d = 12.6$ mm and fitted ϵ_r are shown in Fig. 14. Average estimated permittivity is $1.96 - j0.02$, making it a relatively low loss material for our bands of interest.

C. *Sanded Plywood*

Sanded plywood is a material often used for interior structures and furniture. Our plywood sample is $d = 12.0$ mm thick. The sample was measured both for vertical polarization (E-field parallel to the grain) and horizontal polarization (90° rotation). The sample and fitted ϵ_r are shown in Fig. 15. Average estimated permittivity is $1.71 - j0.083$.

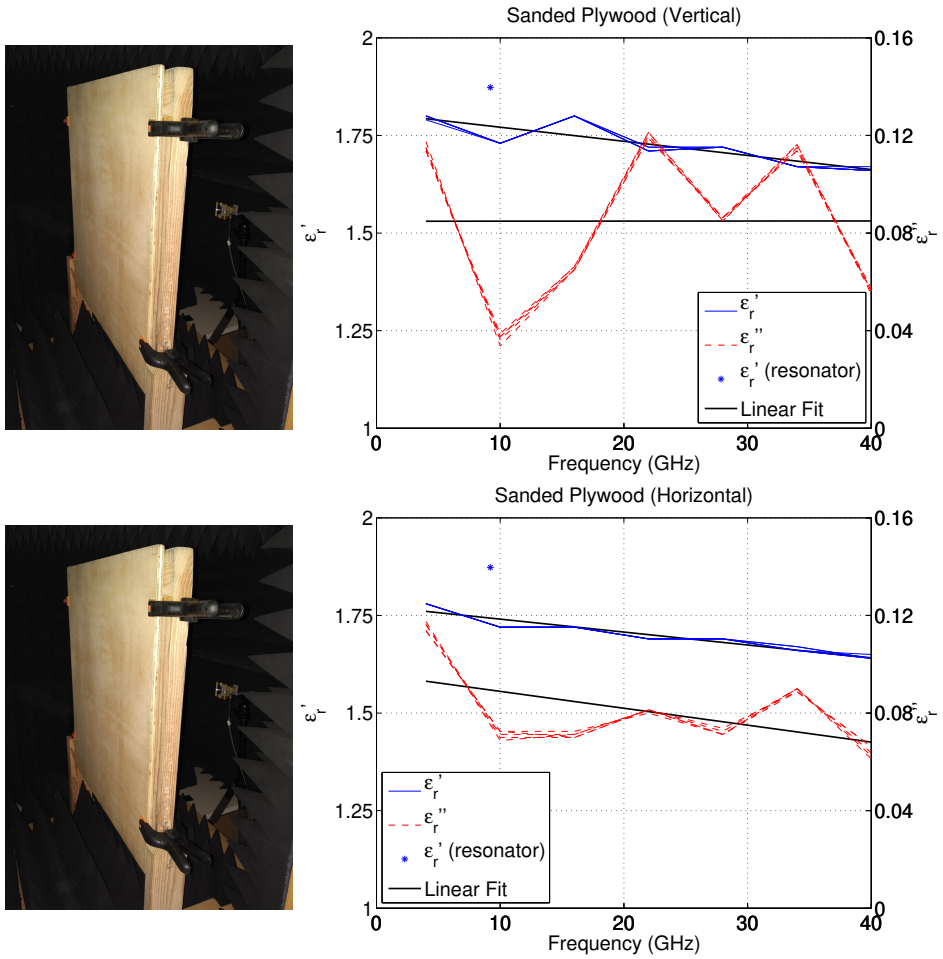

Fig. 15: Extracted complex permittivity of sanded plywood. Two different orientations of the wood were tested, where "vertical" refers to the grain aligned with the incident E-field vector, and "horizontal" refers to a 90-degree rotation.

D. Oriented Strand Board (OSB)

Oriented strand board is a low cost wood panel made from wooden chips that is very popular for outside wall surfaces and roofs in the U.S. Our OSB sample had thickness $d = 15.3$ mm and was measured for both vertical and horizontal polarization as depicted in Fig. 16. Since the chips in OSB seem to have fairly uniform orientation, we arbitrarily call "vertical" polarization the case with the words stamped on the panel right side up, and "horizontal" the case with the words turned $90°$. Average estimated permittivity is $2.03 - j0.10$, representing a somewhat higher loss than our plywood sample.

E. Foam Insulation

Foam insulation is a high-quality insulation material sometimes used instead of the usual fiberglass when robustness to moisture is needed. We measured the $d = 25.2$ mm foam insulation panel type ESR-2142 from Dow Chemical Company as depicted in Fig. 17. The average permittivity is approximately $1.050 - j0.001$, making it a very low loss material in the bands tested.

F. Glass

Untempered glass is commonly used for windows in the U.S. A single sheet of glass (or pane) may be found in older buildings, whereas new installations typically have two or three panes with gaps in between. We measured a single pane of new untempered window glass with $d = 2.22$ mm as depicted in Fig. 18. The average estimated permittivity is $6.86 - j0.14$, representing fairly high loss compared to other materials tested.

G. Red Brick

Red clay brick samples with average thickness 31.3 mm were obtained from Interstate Brick in West Jordan, UT. Bricks were stacked to make a small wall on top of the sample holder as shown in Fig. 19. First, the wall was built with the bricks

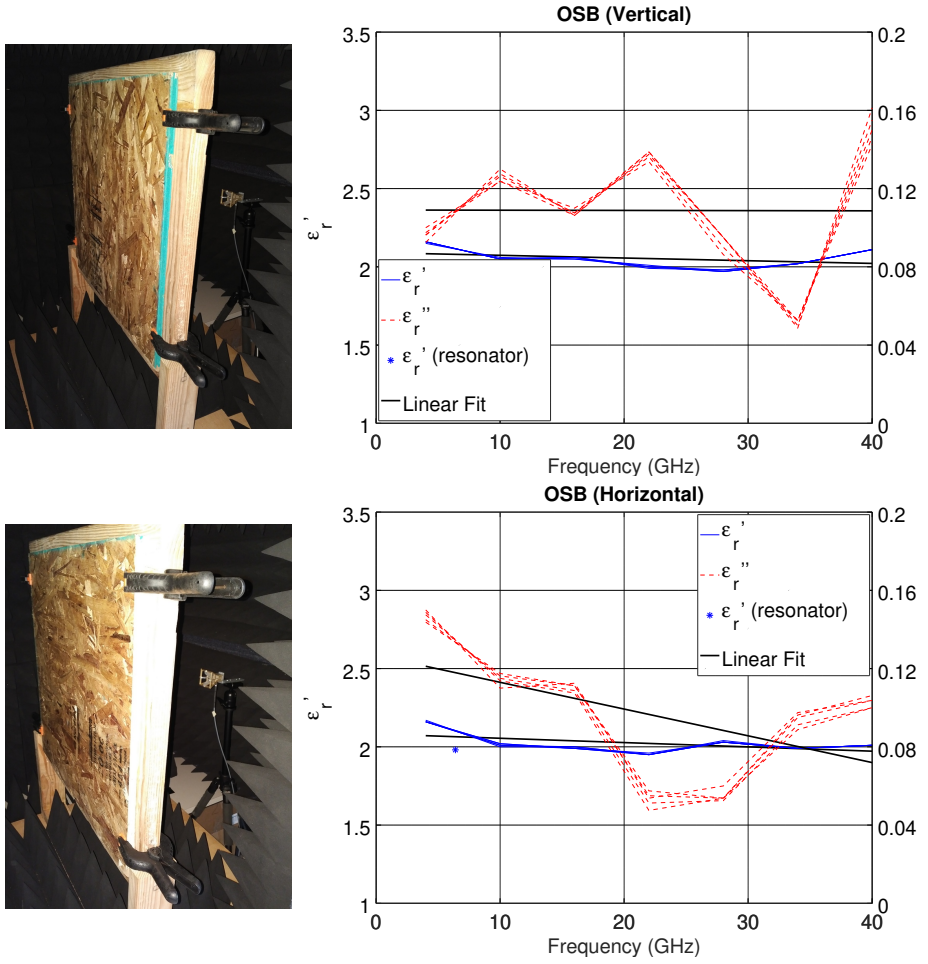

Fig. 16: Extracted complex permittivity of OSB.

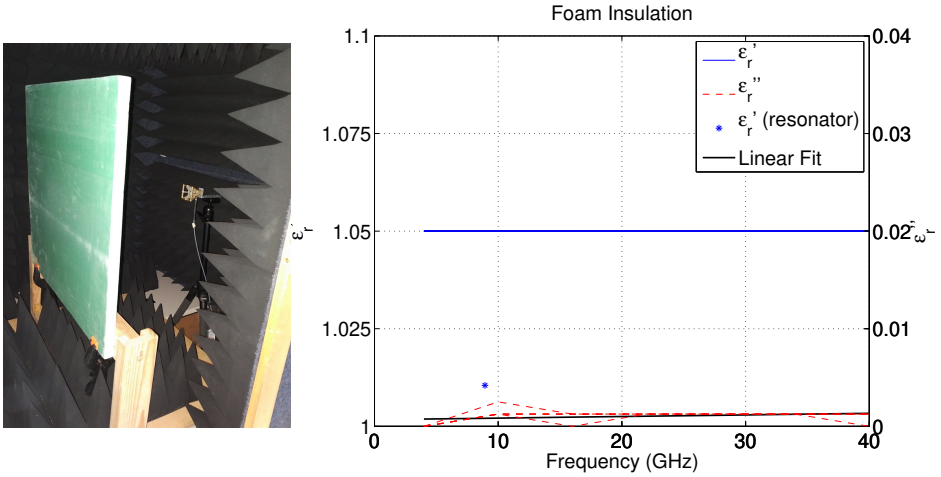

Fig. 17: Extracted complex permittivity of foam insulation.

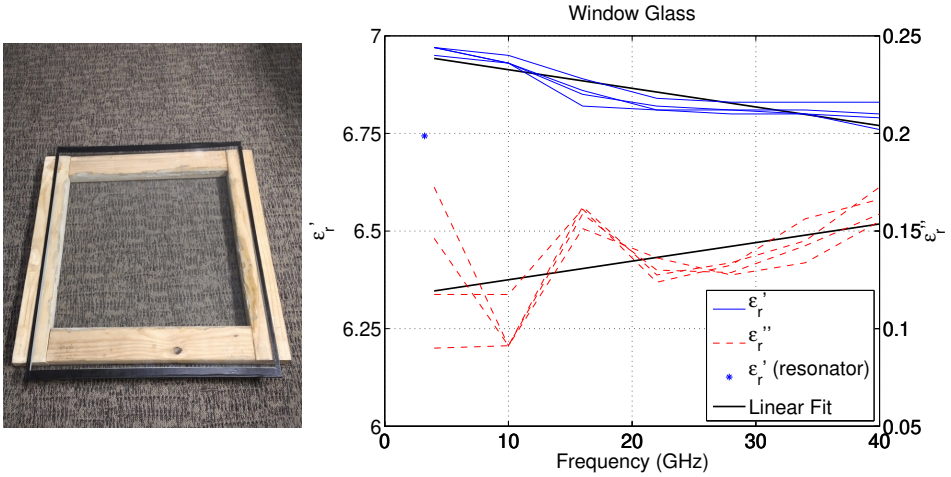

Fig. 18: Extracted complex permittivity of window glass.

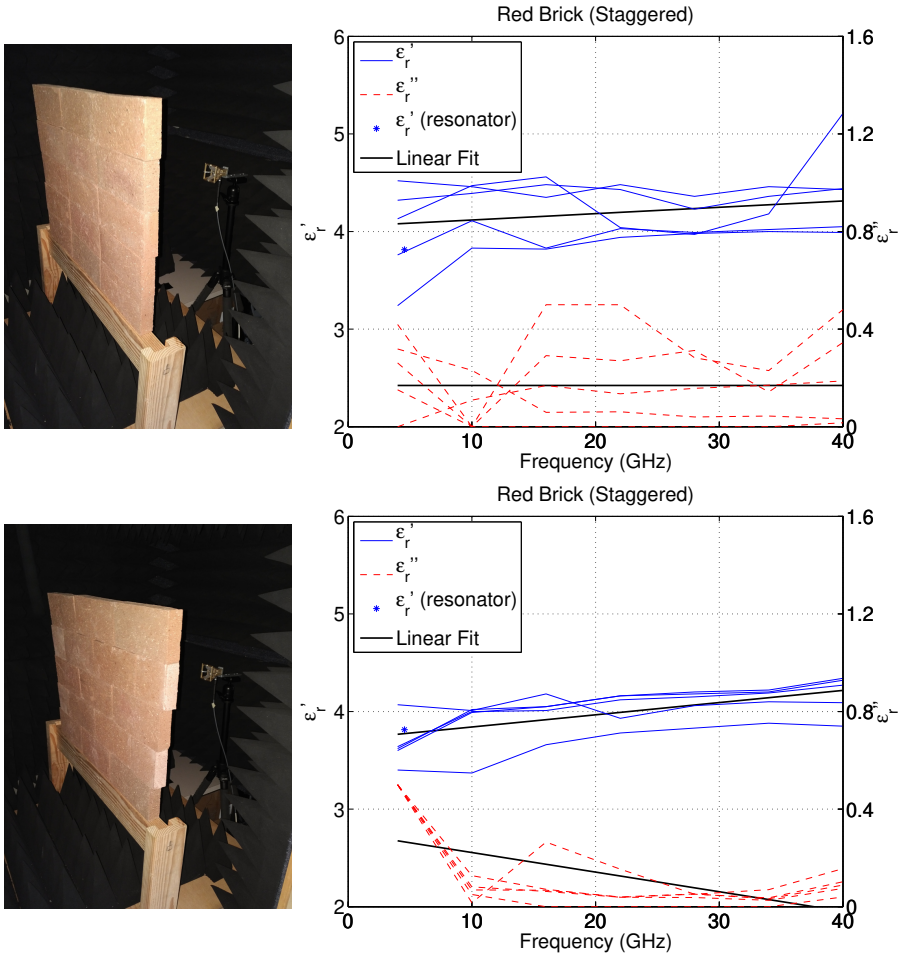

Fig. 19: Extracted complex permittivity of red brick. A small wall was made with a stack of bricks, where the brick edges were aligned (top), or staggered (bottom).

aligned (A) at the edges in each successive layer. Next, brick layers were stacked in a staggered pattern (S). Since for repeated samples, the wall must be rebuilt each time, lower repeatability should be expected compared to samples that come in a single sheet. Interestingly, the staggered arrangement gave more repeatable results than the aligned one. Average estimated permittivity is $4.09 - j0.15$.

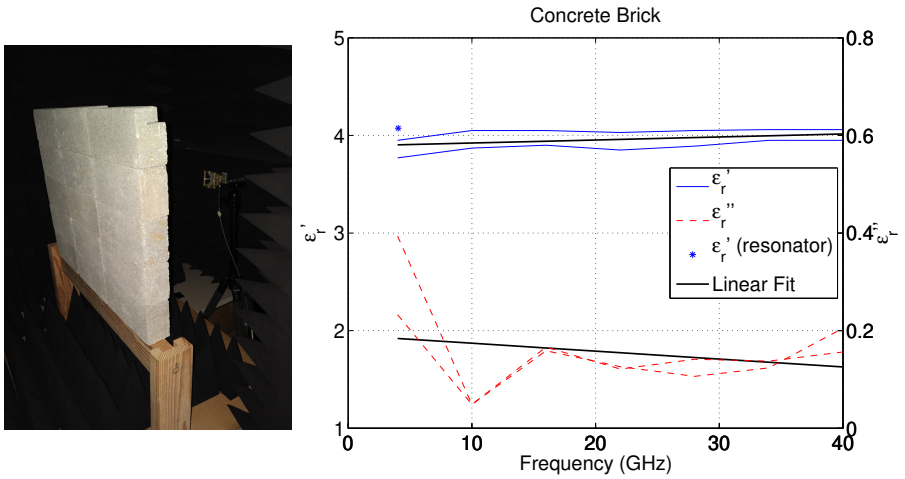

Fig. 20: Extracted complex permittivity of concrete brick. A small wall was made with bricks in an aligned arrangement.

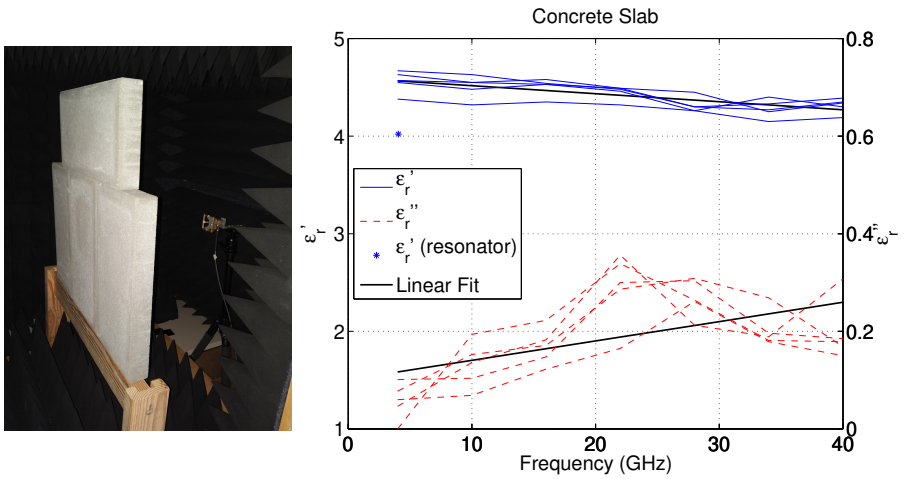

Fig. 21: Extracted complex permittivity of concrete slab. A small wall was built with four slabs as shown.

H. Concrete Brick

We tested concrete "brick" samples, which are concrete blocks that are about the size of a standard brick ($197\times58\times95$ mm^3). The concrete bricks we tested had average thickness $d = 58.6$ mm. The density and composition of the concrete in these bricks appears to be identical to lager hollow concrete masonry units (CMUs) that are often used for foundations in the U.S. Direct measurement of hollow CMUs is difficult with our approach, because of the interior air gaps, and these solid concrete bricks seem to be a good alternative. Only the aligned arrangement of bricks was tested as shown in Fig. 20, and two trials were performed to check repeatability. Average permittivity is $3.96 - j0.16$.

I. Concrete Slab

Solid concrete slabs with average thickness $d = 44.2$ mm were tested as shown in Fig. 21. The composition of the concrete in these slabs appears to be denser than the concrete bricks measured previously, having an appearance more similar to poured concrete. The average estimated permittivity is $4.42 - j0.19$, which is higher than that of the concrete brick samples.

J. Measurement Summary

The linear fit of the extracted permittivities of tested samples are summarized in Table IV.

VI. Conclusion

This report has documented the application of free-space material characterization techniques to common building materials with seamless coverage from 4-40 GHz. A detailed development of the free-space method is also provided. The method is similar to previously reported methods, extended to account for the case of spherical wave spreading, appropriate when using simple horns that do not utilize aperture correcting lenses. We hope that the methods and results herein will be useful to both researchers in material characterization efforts, as well as those needing material parameters for propagation modeling studies.

TABLE IV: Summary of Estimated Complex Permittivity

	Linear Fit		Standard Deviation	
	4 GHz	40 GHz	ϵ_r'	ϵ_r''
Teflon	2.093-j0	2.102-j0	0.0048	0
Drywall	1.980-j0.009	1.945-j0.030	0.0026	0.0009
Plywood (V)	1.792-j0.086	1.663-j0.085	0.0030	0.0012
Plywood (H)	1.760-j0.094	1.641-j0.068	0.0024	0.0010
OSB (V)	2.085-j0.109	2.021-j0.108	0.0039	0.0034
OSB (H)	2.071-j0.122	1.972-j0.072	0.0035	0.0026
Foam	1.050-j0.001	1.050-j0.001	0.0000	0.0003
Glass	6.931-j0.124	6.776-j0.151	0.0152	0.0136
Red Brick (A)	4.079-j0.170	4.313-j0.169	0.3088	0.1453
Red Brick (S)	3.764-j0.270	4.217+j0.019	0.1832	0.0454
Concrete Brick	3.904-j0.184	4.015-j0.126	0.0778	0.0326
Concrete Slab	4.566-j0.117	4.270-j0.259	0.0828	0.0448

ACKNOWLEDGMENT

This work was made possible by equipment provided by NSF MRI grant award number 1725970. We would also like to thank Interstate Brick of West Jordan, UT, for providing free red brick samples for our studies.

REFERENCES

[1] A. Safaai-Jazi, S. M. Riad, A. Muqaibel, and A. Bayram, "Ultra-wideband propagation measurements and channel modeling," DARPA NETEX Program, Tech. Rep., Nov. 2002.

[2] A. Muqaibel, A. Safaai-Jazi, A. Bayram, A. M. Attiya, and S. M. Riad, "Ultrawideband through-the-wall propagation," *IEE Proc. – Microwaves Antennas Propag.*, vol. 152, no. 6, pp. 581–588, Dec. 2005.

[3] Z. Chen and Z. Xiong, "Mitigation of band edge effects in fourier transform based time domain gating," in *Proc. 2019 European Conf. Antennas and Propag.*, Krakow, Poland, Mar. 31 – Apr. 5, 2019, pp. 1–5.

[4] R. G. Geyer, "Dielectric characterization and reference materials," NIST, Tech. Rep. 1338, 1990.

[5] http://www.jonwallace.org.

[6] R. Luebbers, "Lossy dielectrics in FDTD," *IEEE Trans. Antennas Propag.*, vol. 41, pp. 1586–1588, Nov. 1993.

[7] J. W. Wallace, "Modeling electromagnetic wave propagation in electrically large structures," Ph.D. dissertation, Brigham Young University, 2002.

[8] A. M. Eid and J. W. Wallace, "Accurate modeling of body area network channels using surface-based method of moments," *IEEE Trans. Antennas Propag.*, vol. 59, pp. 3022–3030, Aug. 2011.

[9] A. L. Gioia, E. Porter, I. Merunka, A. Shahzad, S. Salahuddin, M. Jones, and M. O'Halloran, "Open-ended coaxial probe technique for dielectric measurement of biological tissues: Challenges and common practices," *Diagnostics*, vol. 8, pp. 1–38, June 2018.

[10] D. Misra, M. Chabbra, B. R. Epstein, M. Microtznik, and K. R. Foster, "Noninvasive electrical characterization of materials at microwave frequencies using an open-ended coaxial line: test of an improved calibration technique," *IEEE Trans. Microwave Theory Tech.*, vol. 38, no. 1, pp. 8–14, Jan. 1990.

[11] J. Baker-Jarvis, R. G. Geyer, J. H. Grosvenor, M. D. Janezic, C. A. Jones, B. Riddle, C. M. Weil, and J. Krupka, "Dielectric characterization of low-loss materials a comparison of techniques," *IEEE Trans. Dielectrics Electrical Insulation*, vol. 5, no. 4, pp. 571–577, Aug. 1998.

[12] J. W. Wallace, "Validation of 4-40 ghz free-space permittivity measurements using dielectric resonators," in *Proc. 2020 IEEE Antennas and Propag. Society Intl. Symp.*, Montreal, Canada, July 7-12, 2020, to appear.

[13] G. Oliver, "Low-loss materials in high frequency electronics and the challenges of measurement," in *EFPL 3rd Annual Workshop on THz Applications in Industry*, Lausanne, Switzerland, Feb. 4, 2015, https://wiki.epfl.ch/thz/2015.